RSC Advances

PAPER

View Article Online
View Journal | View Issue

Check for updates

Cite this: *RSC Adv.*, 2023, **13**, 13477

Bandgap modification in 0D tellurium iodide perovskite derivatives *via* incorporation of polyiodide species†

Benjamin W. Walusiak, Adharsh Raghavan and Christopher L. Cahill *

Halide perovskites provide a versatile platform for exploring the effect of non-covalent interactions, including halogen bonding, on material properties such as band gap, luminescence, and frontier orbital landscape. Herein we report six new zero-dimensional tellurium iodide perovskite derivatives, consisting of $[TeI_6]^{2-}$ octahedra charge balanced by one of several X-Py cations (X = H, Cl, Br, I, and Py = pyridinium). These compounds also feature robust halogen bonding between $[TeI_6]^{2-}$ octahedra and polyiodides in the form of I_2 (**1–4**), I_3^- (**5**), or adjacent octahedra (**4** and **6**). These relatively strong non-covalent interactions (NCIs) are modeled by natural bond order (NBO) and second order perturbation theory (SOPT) calculations. NCIs are responsible for reducing the bandgap of these materials (measured *via* diffuse reflectance spectroscopy) relative to those without polyiodide species. They also affect inner sphere bonding in the metal halide, exacerbating $[TeI_6]^{2-}$ octahedron asymmetry as compared to previously published compounds, with greater asymmetry correlating with higher van der Waals overlap of halogen–halogen contacts. We also demonstrate the ability of hydrogen and carbon bonding (which dominates in the absence of polyiodides) to affect inner sphere tellurium iodide bonding and octahedral symmetry.

Received 13th February 2023
Accepted 21st April 2023

DOI: 10.1039/d3ra00996c

rsc.li/rsc-advances

Open Access Article. Published on 03 May 2023. Downloaded on 2/10/2026 9:29:10 PM.
This article is licensed under a Creative Commons Attribution-NonCommercial 3.0 Unported Licence.

Introduction

Halide perovskites and their derivatives are a class of structurally and functionally diverse materials with relevance to photovoltaics, semiconductors, and radiation detection.[1–3] Our group and others have explicitly shown the potential of non-covalent interactions (NCIs) to influence crystal formation, stability, and material properties (*e.g.* band gap) of perovskites or perovskite derivatives.[4,5] Halogen bonding in particular has also been utilized to improve the stability, quality, and overall efficiency of halide perovskite photovoltaics,[6] and systematic interrogation of new compositions and structural motifs will serve to advance understanding in these areas. Zero-dimensional (0D) halide perovskite derivatives, consisting of entirely discrete metal halide octahedra separated by cations (both organic and inorganic) are increasingly relevant to the applications mentioned above.[7–9] These 0D materials provide a similar platform for tunability of optoelectronic properties, among others, with the tendency toward greater environmental stability, than their three-dimensional counterparts.[10,11] 0D perovskite derivatives are attractive for use as solar materials, and scintillators in particular, which require a high degree of stability while retaining desirable photophysical properties.[6–8] Pb, Sn, Bi, Sb *e.g.* are all frequently explored as components of low dimensional perovskites with properties appropriate for these applications. Tellurium has been probed less extensively than other metals, though it may also form low dimensional compounds with similar characteristics. Te has also been utilized as a dopant in perovskite materials, acting as an emission center in Sn chloride scintillators under X-ray irradiation *e.g.* ref. 12.

Distortion of the metal halide coordination geometry has been shown to be an important factor in determining properties of halide perovskites such as band gap.[13] The identity of the organic cation, halogen on the metal halide, and doping have all been employed to influence the degree of distortion in metal halide octahedra, and subsequently tune their material properties.[13,14] Metal halides with ns^2 lone pairs (Te included, $5s^2$) have also demonstrated distortion in the excited state, which has in turn been tied to their relatively broad emission, *via* the formation of self-trapped excitons (STEs).[15] Since these 0D materials consist of discrete components assembled entirely *via* NCIs, there is significant motivation to characterize these types of interactions in 0D perovskite derivatives. Careful investigation of NCIs such as hydrogen or halogen bonding is essential for establishing relationships between material properties and the non-covalent forces at play in these materials.

Department of Chemistry, The George Washington University, 800 22nd Street, NW, Washington D.C. 20052, USA. E-mail: cahill@gwu.edu

† Electronic supplementary information (ESI) available. CCDC 2238872–2238881. For ESI and crystallographic data in CIF or other electronic format see DOI: https://doi.org/10.1039/d3ra00996c

© 2023 The Author(s). Published by the Royal Society of Chemistry

Open Access Article. Published on 03 May 2023. Downloaded on 2/10/2026 9:29:10 PM. This article is licensed under a Creative Commons Attribution-NonCommercial 3.0 Unported Licence.

Halogen bonding and its influence on material properties

Halogen bonding may be defined as an attractive non-covalent interaction indicated structurally by the interpenetration of the van der Waals volumes of two halogen atoms (usually expressed as a % of the sum of the vdW radii).[16] This phenomenon can arise due to the polarization of a halogen atom covalently bound to another atom, carbon for example, enabling the halogen to act as an electron acceptor.[17] Computational studies have shown that charge transfer from a halogen bond donor to an acceptor can result in a significant stabilization energy between the two species, in addition to the electrostatic interactions arising from polarization of the halogen.[18] Our group has explored the role of NCIs in Te, In, and Sb 0D perovskite derivatives, where we thoroughly characterize these interactions to evaluate their impact on overall structure and material properties.[4,19] These works have demonstrated that second sphere NCIs can substantively affect material properties as well as influence the inner sphere characteristics of the metal halide.

This present effort began as a direct extension of our previous work on Te chlorides and bromides, yet new and unique structural motifs and NCIs presented themselves in this tellurium iodide system. We present a series of new $[TeI_6]^{2-}$ based halide perovskite derivatives paired with halogenated pyridinium cations, and all except for one of these new structures contains polyiodide species, in the form of I_2 or I_3^-. Although this type of polyiodide-containing compound is often reported as an impurity or side product,[20] we take the opportunity here to investigate the significant effect of polyiodides on crystal structure and material properties. These materials feature robust non-covalent interactions (NCIs), including halogen bonding between the polyiodide species and the metal halide, which contribute to the asymmetry of the $[TeI_6]^{2-}$ octahedra. A combination of crystallographic and computational analyses, including natural bond orbitals (NBO), density of states (DOS), and electrostatic potential (ESP) surfaces, allows a comprehensive characterization of the effects of polyiodides on crystal structure and material properties within this series of compounds. The presence of polyiodides substantively affects the band gap of our materials, lowering it in comparison to those without polyiodide species.

Experimental

Reagents were purchased from the following vendors and used as received. Tellurium oxide (TeO_2): Alfa Aesar, hydroiodic acid: BTC chemical, pyridine, 4-chloropyridine hydrochloride, 4-bromopyridine hydrochloride, 4-iodopyridine, pyrazine: Sigma Aldrich.

General synthesis of [1–10]

These efforts represent exploratory, relatively unoptimized syntheses. Herein we rely on *in situ* generation of polyiodides by oxidation of iodide to molecular iodine, which can then combine with additional iodide to form I_3^-.[21] As such, all reactions were performed in air and utilized stabilized hydroiodic acid as the I^- source. Hydrothermal synthesis was employed to aid in the incorporation of I_2 specifically and resulted in the formation of **1–3**. Compounds **4–7** were produced using slow evaporation, rather than hydrothermal methods, and so showed a range of polyiodide incorporation.

Compounds 1–3: $(HXPy)_2[TeI_6]\cdot I_2$ (X = H, Cl, I). The first step in the synthesis of **1–3** was the production of an iodide or polyiodide pyridinium salt. These triiodide XPy salts ($(XPy)[I_3]\cdot H_2O$ X = Cl, Br, I) in particular had not been previously reported in the Cambridge Structural Database (CSD) and are reported herein as compounds **8**, **9** and **10** (powder X-ray diffraction (PXRD), Fig. S10–S12†). 4-X pyridine (XPy) (X = H, I) (0.2 mmol, 0.016 g, 0.042 g) or the HXPy (X = Cl, Br) chloride salt (0.030 g, 0.038 g) was dissolved in 2.0 mL of 2 M stabilized HI and placed in a 23 ml Teflon-lined Parr autoclave. The solutions were heated at 110 °C for 48 hours except for the 4-bromopyridine mixture, which was heated at 70 °C for 48 hours. After cooling to room temperature, the solutions were removed from the autoclaves and allowed to completely evaporate in air. Separately, tellurium oxide TeO_2, (0.1 mmol, 0.016 g) was dissolved in 2.0 mL of 2 M stabilized HI, and dried halopyridinium (I^- or I_3^- salts) material from the previous step was added. This mixture containing tellurium iodide (TeO_2 – >TeI_4 *via* HI, characterized *via* PXRD, Fig. S13†) and the pyridinium was again placed in to a 23 mL Teflon-lined Parr autoclave and heated at 110 °C for 48 hours except for the mixture containing 4-bromopyridinium, which was heated at 70 °C for 48 hours. The resulting liquid–solid mixtures were removed from the autoclave after cooling to room temperature and allowed to dry completely. Black-grey single crystals of **1** and **2**, and silvery-grey single crystals of **3** were extracted from the dried mixtures for single crystal X-ray diffraction. Small amounts of TeI_4 and compounds **8–10** were also present as impurities in some cases, as determined by PXRD.

Compounds 4–6: $(HPyz)_2[TeI_6]\cdot I_2$, $(HClPy)_3[TeI_6(I_3)]$, $(HBrPy)_2[TeI_6]$. Compounds **4–6** were synthesized *via* room temperature reaction of tellurium oxide (TeO_2), 2 M stabilized HI, and pyrazine (pyz) or halopyridinium. Tellurium oxide (TeO_2) (0.1 mmol, 0.016 g), and either HXPy (X = Cl, Br) chloride salt or pyrazine (0.2 mmol, 0.030 g, 0.038 g, or 0.016 g) were mixed with 2.0 mL of 2 M stabilized HI in a 1 dram glass vial. Mixtures were stirred briefly with a spatula and allowed to settle for 24 hours. With these reaction conditions, TeI_4 precipitates from **5** and **6** immediately after mixing. This initial precipitation, and subsequent ingrowth of product phases over time in **5** and **6** is demonstrated by powder X-ray diffraction in the ESI (Fig. S5–S8†). To obtain crystals of **4–6**, solids that had settled at the bottom of the 1 dram vial were separated from the liquid portion after waiting at least 24 hours for product to form. Small single crystals were isolated from this collection of solids for single crystal X-ray diffraction. Evaporation of the separated liquid also yielded single crystals, but of inconsistent composition.

Compound 7: $(HIPy)_2[TeI_6]\cdot H_2O$. Tellurium oxide ($TeO_2$, 0.1 mmol, 0.016 g) and IPy (0.2 mmol, 0.041 g) were mixed with 2.0 mL of 2 M stabilized HI in a 1 dram glass vial. The mixture was stirred with a spatula and the solids allowed to settle for 30 minutes. Aliquots of the dark brown translucent solution were

 © 2023 The Author(s). Published by the Royal Society of Chemistry

Open Access Article. Published on 03 May 2023. Downloaded on 2/10/2026 9:29:10 PM.
This article is licensed under a Creative Commons Attribution-NonCommercial 3.0 Unported Licence.

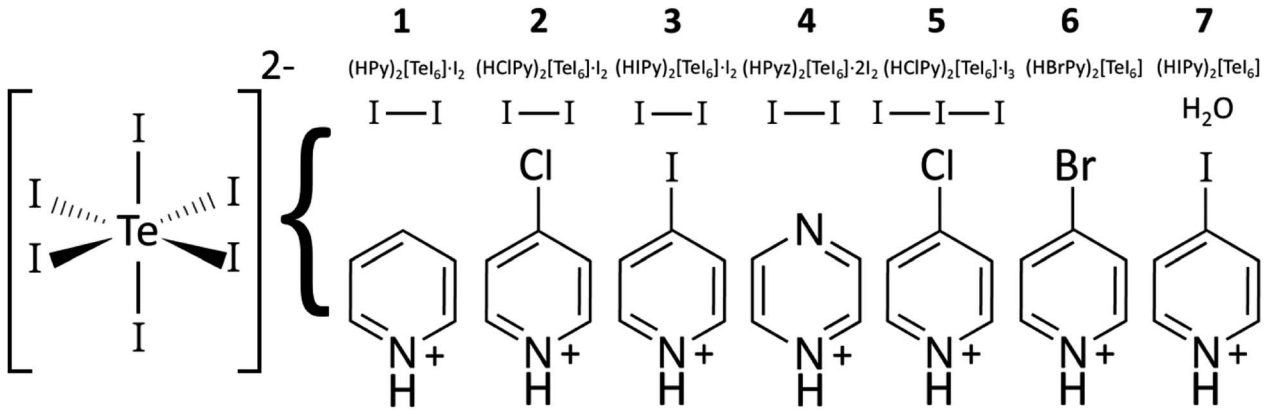

Fig. 1 Diagram of TeI_6 containing compounds 1–7, showing compound number, moiety formula, and presence of I_2, I_3^-, or H_2O if present. While compounds 1–4 were made hydrothermally, 4–7 were made from reactions at room temperature.

pipetted onto a glass slide to evaporate. This yielded a few small black crystals of 7. A graphical summary of compositions **1–7** is shown in Fig. 1.

Compounds 8–10: (HXPy)[I_3]·H_2O (X = Cl, Br, I). Pyridinium triiodide salts (**8–10**, Fig. 2) were also encountered in varying quantities as side products in nearly all syntheses involving XPy and HI. These compounds were prepared directly, however, by the first step of the method described for **1–3:** 2.0 mL of stabilized HI was mixed with 0.2 mmol XPy·HCl (X = Cl, Br), 0.030 g, 0.038 g, or IPy, 0.041 g, and allowed to dry in air. Hydrothermal treatment of XPy and 2 M stabilized HI also yields I_3^- Py salts. The resulting brown solid was used as a starting material for **1–3**. Lower solubility of unprotonated IPy may require a larger volume or multiple treatments of HI more fully convert to the I_3^- salt. PXRD also revels the presence of some amount of (HXPy)[I], a colorless translucent solid, which can be easily distinguished from the brown **8–10**. Crystal structures and descriptions for **8–10** can be found in the ESI.† We note that the use of unstabilized HI may also produce compounds **1–5**, and **8–10** since it contains some unknown quantity of polyiodides due to its age and exposure to air. Unstabilized HI was used in our initial exploratory synthesis efforts, which were somewhat unpredictable with very low yields in some cases. We suggest the synthesis of **1–10** may be further optimized by combining controlled amounts of iodide salts and dissolved I_2, as has been utilized for systematic incorporation of polyiodides into lead based perovskites.[22] Such control over the polyiodide content may allow better control of products and impurities.

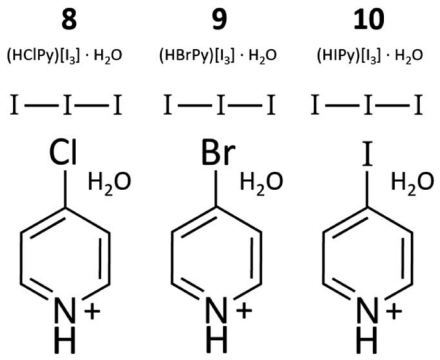

Fig. 2 Diagram of 8–10, which consist of I_3 paired with HXPy (X = Cl, Br, I). These are also the main impurity phases in 1–7.

X-ray crystallography

Crystals of **1–10** were harvested from dried products or filtered solids and mounted on MiTeGen micromounts. All measurements were made using monochromated microfocus Mo Kα (λ = 0.71073 Å) radiation on a Bruker D8 Quest, equipped with a Photon II detector. All reflections were collected at 100(2) K with 0.5° φ and ω scans. Initial space group determination was performed using a single φ scan in the APEX III software suite. The data were reduced using SAINT[23] and empirical absorption correction applied using SADABS.[24] Structures solutions, solved using intrinsic phasing, and refinement were performed using the ShelXT package[25] and ShelXL[26] in APEX III. ShelXle,[26] OLEX 2,[27] and PLATON[28] programs were used for subsequent refinement, modeling of disorder, and space group changes when necessary. All atoms were refined anisotropically, and aromatic hydrogen atoms were placed in idealized positions using the appropriate AFIX command and allowed to ride on the coordinates of the parent atom with isotropic thermal parameters (U_{iso}) fixed at 1.2 U_{eq}. Specific crystal structure parameters of **1–10** are summarized in Table 1. CheckCIF documents containing thermal ellipsoids (generated *via* ORTEP[29]) for **1–10** can be found in the ESI.†

A noticeable gap in our suite of materials is present in that the TeI_6 + BrPy analogue containing I_2 is not reported above. Like **1–3**, hydrothermal syntheses (at 70 °C) involving tellurium and BrPy did yield single crystals, however these structures could not be adequately refined. In the $P3_2$ trigonal space group, 8 twin domains are possible simply due to the symmetry of the system.[30] Despite the application of several simultaneous twin laws to try and resolve the merohedral twinning issue, a satisfactory refinement was not obtained. However, powder X-ray diffraction (PXRD, Fig. S12†) revealed the presence of a compound nearly identical to **3** in syntheses attempting to make $(HBrPy)_2[TeI_6]\cdot I_2$. It is therefore reasonable to surmise that the structure of $(HBrPy)_2[TeI_6]\cdot I_2$ is analogous to that of **3**.

Open Access Article. Published on 03 May 2023. Downloaded on 2/10/2026 9:29:10 PM.
This article is licensed under a Creative Commons Attribution-NonCommercial 3.0 Unported Licence.

Table 1 Crystallographic data table for compounds **1–10**

	1	**2**	**3**	**4**	**5**
CCDC no.	2238872	2238873	2238874	2238875	2238876
Formula	$(C_5H_5NH)_2[TeI_6]\cdot I_2$	$(C_5H_5NCl)_2[TeI_6]\cdot I_2$	$(C_5H_5NI)_2[TeI_6]\cdot I_2$	$(C_4H_6N_2)_2[TeI_6]\cdot 2(I_2)$	$(C_5H_5NCl)3[TeI_6]\cdot I_3$
Crystal system	Monoclinic	Monoclinic	Trigonal	Triclinic	Triclinic
Space group	$C2/c$	Cc	$P3_2$	$P\bar{1}$	$P\bar{1}$
a (Å)	18.0503(11)	19.0162(14)	15.0194(10)	9.4074(3)	8.9408(3)
b (Å)	10.1185(6)	10.6017(8)	15.0194(10)	11.5528(4)	9.9568(4)
c (Å)	14.6269(8)	14.2508(11)	33.038(3)	13.8021(4)	19.7612(8)
α (°)	90	90	90	81.7110(10)	103.0060(10)
β (°)	106.830(2)	111.154(3)	90	79.8470(10)	96.6570(10)
γ (°)	90	990	120	69.0100(10)	90.2810(10)
Volume (Å^3)	2557.06	2679.42	6454.31	1373.2	1701.62
Z	4	2	3	4	4
ρ_{calc} (g cm^{-3})	3.385	3.401	3.6	3.77	3.149
Radiation	0.71073	0.71073	0.71073	0.71073	0.71073
Temp. (K)	100	100(2)	100(2)	100(2)	100(2)
Residuals: R (R_{int})	0.0305, 0.0584	0.0348, 0.0601	0.0242, 0.0963	0.0200, 0.0426	0.0340, 0.0426

	6	**7**	**8**	**9**	**10**
CCDC no.	2238877	2238878	2238879	2238880	2238881
Formula	$(C_5H_5NBr)_2[TeI_6]$	$(HIPy)_2[TeI_6]\cdot H_2O$	$(HClPy)[I_3]\cdot H_2O$	$(HBrPy)[I_3]\cdot H_2O$	$(HIPy)[I_3]\cdot H_2O$
Crystal system	Monoclinic	Triclinic	Triclinic	Monoclinic	Monoclinic
Space group	$P2_1/n$	$P\bar{1}$	$P\bar{1}$	$C2/c$	$C2/c$
a (Å)	12.1949(6)	7.7588(4)	7.0961(3)	22.6882(7)	22.8618(8)
b (Å)	14.1651(7)	11.8319(4)	7.8772(3)	7.0484(2)	7.1336(2)
c (Å)	14.3164(7)	14.2751(8)	11.4958(5)	15.6003(5)	15.7192(6)
α (°)	90	86.842(2)	95.461(2)	90	90
β (°)	110.829(2)	80.992(2)	99.379(2)	101.8650(10)	103.2200(10)
γ (°)	90	78.3800(10)	107.782(2)	90	90
Volume (Å^3)	2311.42	1267.41	592.48	2441.43	2495.66
Z	4	2	2	8	8
ρ_{calc} (g cm^{-3})	3.469	3.456	2.858	3.3035	3.219
Radiation	0.71073	0.71073	0.71073	0.71073	0.71073
Temp. (K)	100(2)	100(2)	100(2)	100(2)	100(2)
Residuals: R (R_{int})	0.0208, 0.0765	0.0203, 0.0469	0.0264, 0.0600	0.0223, 0.0422	0.0167, 0.0422

Photophysical measurements

Diffuse reflectance spectra were collected on solid, dry samples at 298 K. Spectra were collected from 200 nm to 1500 nm on a Jasco V-770 UV-visible/NIR spectrophotometer equipped with a 60 mm integrating sphere (Jasco ISN-923). Data were processed using Spectra Manager™ Suite spectroscopy software. Steady-state luminescence scans of **1–3** and **5** were collected at 298 K and 78 K with a Fluorologs-3 photoluminescence spectrophotometer from Horiba using a 450 W xenon arc lamp combined with a double excitation monochromator and double emission monochromator, with a photomultiplier tube at 950 V used as the emission detector. Low temperature luminescence measurements were collected on solid samples under vacuum using a Janis VPF-100 cryostat equipped with UV-grade fused silica windows coupled with a Lakeshore model 325 temperature controller.

Computational methods

Natural bond orbital (NBO) analyses, including second order perturbation theory (SOPT) calculations, were performed using the NBO7 package as implemented in Gaussian 16, rev. C.01.[31] The model chosen for NBO calculations consisted of a central $[TeI_6]^{2-}$ species and its vdW or near-vdW contacts, including organic cations and other molecular species. The coordinates of all atoms were taken from the single crystal X-ray diffraction data for each compound. Single point energy (SPE) calculations were performed using the B3LYP[32,33] functional and the def2-tzvp[34,35] basis set for all atoms (with effective core potential (ECP) for I and Te).

Density of states (DOS) and SPE calculations incorporating periodic boundary conditions (PBC) were performed using Gaussian 16, rev. C.01 on crystallographically determined unit cells, using the HSEh1PBE[36] functional and the basis sets def2-tzvp for Cl, Br, I and Te (with ECP for I and Te), and 6-311G** (ref. 37 and 38) for C, H and N atoms. Total and partial density of states (TDOS, PDOS) data were extracted using Multiwfin v3.7.[39] Individual PDOS fragments were generated using appropriate atomic orbital contributions (s and p orbitals of Te, I, Cl and Br atoms, and p orbitals of C and N atoms). DOS curves were plotted at a FWHM of *ca.* 0.25 eV.

© 2023 The Author(s). Published by the Royal Society of Chemistry

Open Access Article. Published on 03 May 2023. Downloaded on 2/10/2026 9:29:10 PM.
This article is licensed under a Creative Commons Attribution-NonCommercial 3.0 Unported Licence.

Elemental analysis

Elemental analysis was performed on all compounds by Atlantic Microlab, Inc. for C, H, N, and I. Results are tabulated in Table S3.†

Results and discussion

Structure descriptions

Compounds 1–3 $(HXPy)_2[TeI_6]\cdot I_2$ (X = H, Cl, I). Compounds **1–3** contain polyhalide (I_2) molecules, and have a generic formula of: $(HXPy)_2[TeI_6]\cdot I_2$ where X = H, Cl, I. The structures consist of $[TeI_6]^{2-}$ octahedra linked to I_2 molecules *via* halogen bonding, and $HXPy^+$ units linked to other substituents *via* hydrogen and halogen bonding. The basic coordination environment of the metal halide octahedron is very similar for **1–3**. Each $[TeI_6]^{2-}$ octahedron participates in halogen bonding with its six closest I_2 molecules, with each tellurium bound iodine interacting with one I_2 molecule, adopting one of two possible arrangements (Fig. 3). These halogen bonding interactions could be thought of as type I (end-on) and type II (side-on) interactions geometrically speaking.[40] However, the nature of these end-on $[TeI_6]^{2-}\cdots I_2$ halogen bonds, including the presence of charge transfer behavior, does not strictly fit the standard type I halogen bond definition,[40] and details of this interaction are further explained in the computational section. There are also halogen bonds between the halogen substituent on the Py and the $[TeI_6]^{2-}$ in the case of **2** and **3**. Each I_2 molecule is in turn halogen-bonded to the six nearest $[TeI_6]^{2-}$, creating a 3D halogen-bonded framework which can be seen in Fig. S14.†

Compound **1** $(HPy)_2[TeI_6]\cdot I_2$ has been reported previously by Faoro *et al.*, during the investigation of aryltellurenyl iodides, although with slightly different crystallographic parameters, likely due to the difference in collection temperatures (293 K *vs.* 100 K).[41] Compound **1** (Fig. 4) crystallizes in the *C*2/*c* space group, and the average Te–I bond length is 2.940(1) Å, with min. and max. I–Te–I angles of 87.5° and 92.4° respectively. As in all compounds presented here, **1** consists of $[TeI_6]^{2-}$ octahedra charge-balanced by organic cations and features discrete I_2 molecules halogen bonded with the $[TeI_6]^{2-}$. For brevity, we will describe the strongest halogen bonding interactions in each compound, which for **1–3** occur between end-on bound I_2 molecules and the $[TeI_6]^{2-}$. For **1**, a single crystallographically unique end-on I_2 is present with a Te–I$\cdots I_2$ distance of 3.252(1) Å. This represents a significant overlap of the van der Waals (vdW) radii of the Te bound iodine and the I_2 iodine, 82.1% of the sum of the vdW radii (hereafter expressed as % vdW).[42] In contrast, halogen bonding distances between $[TeI_6]^{2-}$ and side-on I_2 are ~98% vdW. More insight into the nature of this rather robust interaction is given in the computational results section. Hydrogen bonding also contributes to the overall assembly of **1–7**, and is present in **1–3** between $[HXPy]^+$ and $[TeI_6]^{2-}$.

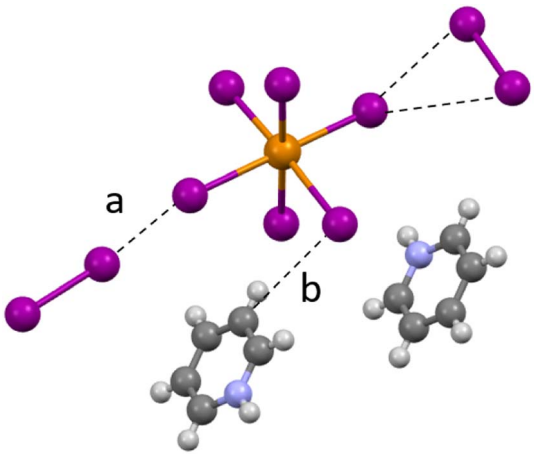

Fig. 4 A portion of the structure of **1** showing (a) halogen bonding and (b) hydrogen bonding between I_2 and pyridinium species.

Compound **2** $(HClPy)_2[TeI_6]\cdot I_2$ (Fig. 5) exhibits a similar second sphere coordination environment as **1**, crystallizing in the lower symmetry *Cc* space group. The average Te–I bond length is 2.947(1) Å, with min. and max. I–Te–I angles of 85.9° and 93.2° respectively. The closest halogen–halogen contacts are once again the two end-on coordinated I_2 molecules with

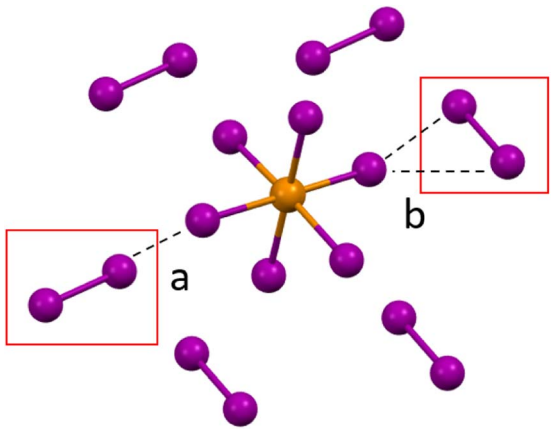

Fig. 3 a. Halogen bonding in compounds **1–3** between the $[TeI_6]^{2-}$ octahedron between end on (a) and side on (b) I_2 molecules.

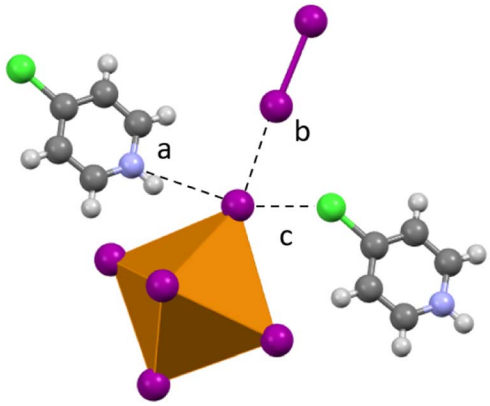

Fig. 5 Second sphere interaction in 2. (a) Hydrogen bonding; (b) and (c) halogen bonding between the $[TeI_6]^{2-}$ octahedron and an end-on I_2 and ClPy respectively.

Open Access Article. Published on 03 May 2023. Downloaded on 2/10/2026 9:29:10 PM. This article is licensed under a Creative Commons Attribution-NonCommercial 3.0 Unported Licence.

Te–I···I_2 distances of 3.287(1) Å and 3.353(1) Å, 83.0% and 84.7% vdW respectively. The Cl substituent on the chloropyridinium is just beyond overlapping with the vdW radius of the tellurium bound iodine, with a Cl···I distance of 3.740(1) Å, or 100.3% vdW. Fig. 5 shows examples of each type of non-covalent interaction present.

Compound **3** $(HXPy)_2[TeI_6]\cdot I_2$ crystallizes in the $P3_2$ space group, a stark departure from monoclinic space groups of **1** and **2**. Nevertheless the $[TeI_6]^{2-}$ octahedra in **3** retain the same second sphere coordination as **1** and **2**. The average Te–I bond length is 2.954(1) Å, with min. and max. I–Te–I angles of 85.41° and 93.59° respectively. Due to the symmetry of **3**, there are 3 crystallographically unique $[TeI_6]^{2-}$ octahedra (Fig. S15†), so an average of their closest (end on) Te–I···I_2 coordination distances were taken for the purpose of comparison. These distances are 3.367(1) Å and 3.394(1) Å, 85.0% and 85.7% respectively. Iodine atoms on multiple iodopyridiniums were modelled as disordered, indicating a disorder of the entire pyridinium molecule.

Compound **4** $(HPyz)_2[TeI_6]\cdot I_2$ crystallizes in the $P\bar{1}$ space group and exhibits a completely different second sphere coordination from **1–3** (Fig. 6). In this new arrangement, there are still I_2 molecules involved in halogen bonding with the $[TeI_6]^{2-}$, the shortest of which is 3.316(1) Å, 83.7% vdW. There is also halogen bonding present between the I atoms on adjacent $[TeI_6]^{2-}$, with the closest contact being 3.582(1) Å, 90.5% vdW. $[TeI_6]^{2-}$ octahedra are charge balanced by infinite 1D chains of singly protonated pyrazine molecules hydrogen bonded to one another end to end, with additional hydrogen bonding to both I_2 and $[TeI_6]^{2-}$. Like **1–3**, the $[TeI_6]^{2-}$ octahedron is slightly distorted, with an average Te–I bond length of 2.949(1) Å and min. max. I–Te–I angles of 86.48° and 95.88° respectively. This compound demonstrates the diversity of potential second sphere coordination environments around the $[TeI_6]^{2-}$ while still retaining a large vdW overlap between the tellurium iodide and the I_2. We wish to highlight the robust nature and variety of the $[TeI_6]^{2-}\cdots I_2$ halogen bonding in compounds **1–4** in general, while not discounting that hydrogen bonding also plays a role in the assembly of these compounds.

Compound **5** $(HClPy)_3[TeI_6(I_3)]$ crystallizes in the $P\bar{1}$ space group and modification of synthesis parameters results in the inclusion of I_3^- rather than I_2. Analogous to **1–4**, halogen bonding occurs between the I_3^- species and the $[TeI_6]^{2-}$ in both side-on and end-on arrangements (Fig. 7). A somewhat smaller degree of van der Waals overlap occurs between I_3^- and $[TeI_6]^{2-}$, compared to the larger overlap present in the end-on I_2 interactions in **1–3**. Relevant distances and angles for the end on halogen interaction (Te–I···I_3^-) in **5** are: 3.630(1) Å, 91.67% vdW. Side-on I_3^- interactions have a lesser vdW overlap of ~97%, again analogous to **1–3**. The average Te–I bond length is 2.937(1) Å and min. and max. I–Te–I angles of 87.17° and 91.86° respectively.

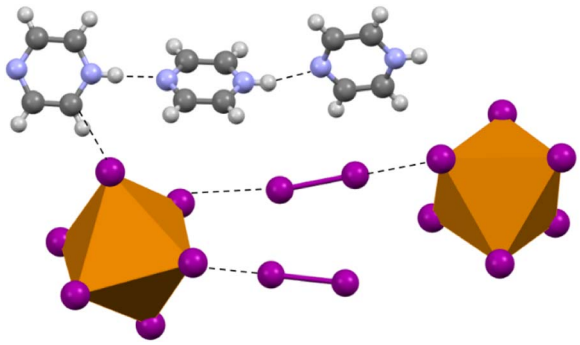

Fig. 6 Selection from the structure of **4** showing the overall coordination environment, both halogen and hydrogen bonding, in contrast to compounds **1–3**.

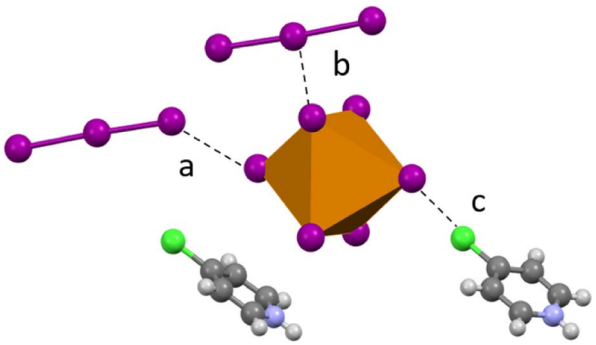

Fig. 7 Examples of second sphere interactions in **5**: halogen bonding between the $[TeI_6]^{2-}$ and an (a) end-on I_3, (b) side-on I_3, and (c) chlorine substituent on the pyridinium.

I_3^- containing crystal structures are sometimes reported as side products in the literature, with an example being (dimethylammonium)$_3[PtI_6(I_3)]$ by Evans *et al.*[20] a study focused on mainly compunds containg I_2. A search of the Cambridge Structural Database (CSD) reveals only a single (divalent) tellurium halide containing I_3^- ($(C_3H_{10}N)_2[Te(2+)I_4]$) and no structures combining Te(4+) and I_3^-. Compound **5** therefore represents a rarely reported structural motif for Te halide based materials. As with I_3^-, many authors seem to first encounter I_2 containing materials pursing other products, as reported by Faoro *et al.*[41] This precedent should not diminish the importance of polyiodides, as the presence of I_2 has been demonstrated to play a role in the defect chemistry of the well-known halide perovskite $MAPbI_3$, as well as in the degradation pathway of Sn based perovskite solar cells.[41,43,44] Additionally, polyhalide rich solutions have recently been utilized as a crystallization aid in halide perovskite based solar cells.[45] The presence of discrete I_2 molecules has also been reported before in Pt halides, yet this study emphasized hydrogen bonding between I_2 and the organic cations, referencing halogen bonding only in passing.[20] In our case, the organic molecules do not seem to systematically complement or template the positions of I_2 in the crystal. We instead call attention to the robust $I_2\cdots[TeI_6]^{2-}$ halogen bonds present in **1–5**. Novikov *et al.* focused on the properties of photovoltaic devices made with polyiodide containing materials, while noting the role of halogen bonding between I_2 and $[TeBr_6]^{2-}$ in assembling their materials. Considering these observations, we see an opportunity to advance our understanding of the halogen bonding interactions between the I_2 and metal halide. Compounds **1–6** provide a platform to

© 2023 The Author(s). Published by the Royal Society of Chemistry

Open Access Article. Published on 03 May 2023. Downloaded on 2/10/2026 9:29:10 PM.
This article is licensed under a Creative Commons Attribution-NonCommercial 3.0 Unported Licence.

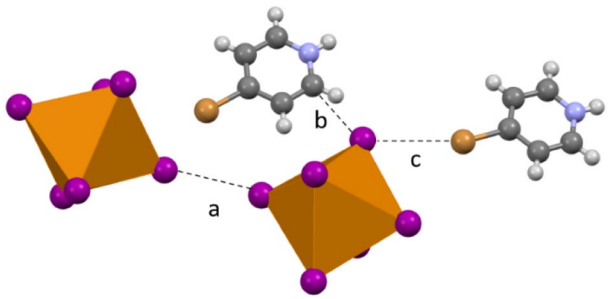

Fig. 8 Subset of second sphere interactions in **6**: (a) halogen bonding between two $[TeI_6]^{2-}$ (b) hydrogen bonding and/or carbon bonding between BrPy and $[TeI_6]^{2-}$ and (c) halogen bonding between $[TeI_6]^{2-}$ and bromine substituent on the pyridinium.

systematically probe the effects of polyiodides and halogen bonding on structure and material properties.

Compound **6** $(HBrPy)_2[TeI_6]$ crystallizes in the $P2_1/n$ space group and contains no polyiodide species owing to changes in synthesis detailed in the experimental section. As in **2–5** there is halogen bonding between the BrPy and the $[TeI_6]^{2-}$, with a Br⋯I distance of 3.758(1) Å (98.12% vdW). There is also halogen bonding between adjacent $[TeI_6]^{2-}$ units, with the shortest Te–I⋯I–Te distance being 3.801(1) Å (96.0% vdW). (Fig. 8). The average Te–I bond length is 2.944(1) Å with min. and max. I–Te–I angles of 86.6° and 93.4° respectively. In addition, compound **6** exhibits carbon bonding,[46] where the interaction is between the halogen donor and C=C or C=N σ* bonds in $[HXpy]^+$, as opposed to the C–H or N–H bond σ*, is present along with normal hydrogen bonding. The Te–I⋯C distance (see Fig. 8b) is 3.489(1) Å additional details on this interaction can be found in the computational section.

Compound **7** $(IPy)_2[TeI_6]\cdot H_2O$ crystallizes in the $P\bar{1}$ space group and exhibits halogen bonding with the IPy is present (Fig. S18†), with the later having an I⋯I distance of 3.836 (1) Å (96.9% vdW). There is also halogen bonding between adjacent $[TeI_6]^{2-}$ units, with the shortest Te–I⋯I–Te distance being 3.830(1) Å (96.7% vdW). Unlike **1–5**, **7** does not contain polyiodides, but rather an H_2O molecule, highlighting the possible diversity of the tellurium iodide – pyridinium system. Due to its low yield during synthesis **7** is excluded from most subsequent analyses.

Compiled crystallographic metrics

$[TeI_6]^{2-}$ asymmetry. The internal symmetry of the metal-halide polyhedron plays an important role in determining the resultant material properties of 0D perovskites in particular,[47–49] and a distortion metric (Δd) is commonly used to quantify the deviation of each metal-halide bond length from an ideal octahedral geometry (Table 2).[50] Depending on the system, $[TeX_6]^{2-}$ octahedra can be completely symmetric, as is the case for inorganic cubic compounds such as Cs_2TeX_6 (X = Cl, Br, I),[51] yet in cases where the packing environment of the $[TeX_6]^{2-}$ octahedron is of lower symmetry, the octahedron itself becomes distorted to varying degrees. A survey of crystal structures from the Cambridge Structural Database (CSD) containing $[TeI_6]^{2-}$ octahedra yielded 34 compounds with varying levels of distortion in the octahedron. Among the most distorted were $((C_{22}H_{20}O_2P)_2[TeI_6]$, space group $P\bar{1}$) and $((C_{19}H_{18}P)_2[TeI_6]$ space group $C2/c$), which have Δd values of 1.68×10^{-4} and 1.58×10^{-6} respectively.[52,53] In these hybrid organic–inorganic compounds, only hydrogen bonding between the organic components and the metal halide is present. Numerical values for *our* compounds range from as low as $\sim 10^{-6}$ (for previously reported $[TeCl_6]^{2-}$ and $[TeBr_6]^{2-}$ based compounds) to as high as $\sim 10^{-3}$ in compounds **1–6** reported here (Table 2). **1–6** have a much larger distortion metric than any $[TeI_6]^{2-}$ containing compound present in the CSD, and also larger than our previously reported $[TeCl_6]^{2-}$ and $[TeBr_6]^{2-}$ based materials. The distortion metric in **1–6** tends to increase as the halogen bond between $[TeI_6]^{2-}$ and end-on I_2 species becomes shorter (lower % in Table 2). These data suggest that halogen bonding may increase distortion of the metal halide octahedron, beyond what has been observed to arise due to an asymmetric packing environment and hydrogen bonding with $[TeI_6]^{2-}$. We therefore call attention to the potential utility of this polyiodide halogen bonding motif to affect the distortion of metal halides. Additional metrics involving octahedral distortion can be seen in subsequent sections.

Luminescence

Compounds **1–6** were not found to be luminescent at room temperature or at 77 K. All inorganic tellurium halides, *e.g.* Cs_2TeX_6 (X = Cl, Br, I) exhibit luminescence output with

Table 2 Halogen bonding overlap and distortion metrics for compounds **1–6**. Distortion metric is defined as: $\Delta d = \frac{1}{6}\sum_{n=1,6}\left(\frac{d_m - d_{ave}}{d_{ave}}\right)^2$, where d_m is a metal-halogen distance and d_{ave} is the average M–X distance

Compound	Chemical formula	Closest halogen vdW overlap %	Distortion metric (Δd)
1	$(HPy)_2[TeI_6]\cdot I_2$	82.1	1.49×10^{-3}
2	$(HClPy)_2[TeI_6]\cdot I_2$	83.0	1.39×10^{-3}
3	$(HIPy)_2[TeI_6]\cdot I_2$	85.0	1.01×10^{-3}
4	$(HPyz)_2[TeI_6]\cdot I_2$	83.7	6.78×10^{-4}
5	$(HClPy)_3[TeI_6]\cdot I_3$	91.2	3.72×10^{-4}
6	$(HBrPy)_2[TeI_6]$	98.1	6.54×10^{-4}
$SOSYEG_{30}$	$(C_{22}H_{20}O_2P)_2[TeI_6]$	n/a	1.68×10^{-4}
$IRIHEW_{31}$	$(C_{19}H_{18}P)_2[TeI_6]$	n/a	1.58×10^{-6}
$OMOLEK_4$	$(HIPy)_2[TeCl_6]$	92.6	4.61×10^{-6}
$OMOMAH_4$	$(HIPy)_2[TeBr_6]$	92.2	3.45×10^{-6}

© 2023 The Author(s). Published by the Royal Society of Chemistry

Open Access Article. Published on 03 May 2023. Downloaded on 2/10/2026 9:29:10 PM. This article is licensed under a Creative Commons Attribution-NonCommercial 3.0 Unported Licence.

intensities varying as Cl > Br ≫ I.[51,54] Our previous work with tellurium chloride and bromide halo pyridiniums found that their luminescence is only significant at low temperature (~77 K), and is sometimes not present at all.[4] The combined presence of pyridinium cations and polyiodides, especially considering the intimate second sphere contacts present in **1–5**, likely provides multiple pathways for non-radiative decay of the excited $[TeI_6]^{2-}$. Besides eliminating polypodies, other organic cations besides pyridine could be potentially utilized in an attempt to improve luminescent behavior. Biswas *et al.* noted that benzyltriethylammonium, in contrast to various other organic cations, resulted in high room temperature photoluminescence quantum yield of a hybrid organic–inorganic tellurium chloride. Lack of luminescence does not preclude the possible use of these materials as potential direct radiation detectors or photovoltaic devices *e.g.*, where electron hole pairs are detected by a supporting device without the need for emission of photons.[7,55,56]

Computational analysis: NBO, ESP, DOS

As crystallographic metrics strongly indicated the presence of robust halogen bonding as described above, natural bond order (NBO), density of states (DOS), and electrostatic potential surfaces (ESP) were utilized to quantify and visualize the nature of these interactions and investigate the frontier orbital landscape of our materials. In this work, we wish to employ our computational analyses to rigorously evaluate the consequences of the presence of polyiodides, obtain an orbital level understanding of the robust halogen bonding interactions between I_2 or I_3^- and $[TeI_6]^{2-}$, and investigate any resultant effects on material properties. Studies of other polyiodide containing systems, such as those undertaken by Adonin *et al.*, have utilized some computational analysis in the form of QTAIM (quantum theory of atoms in molecules) to obtain electron density maps of similar NCIs in bismuth iodides.[57] Owing to the intimate nature of halogen bonds in our materials, we sought to probe these interactions in several ways to better understand their effects.

Table 3 Details of most intimate halogen–halogen interactions for compounds **1–6** noting interacting species, vdW %, and calculated stabilization energy of the interaction

Compound	Halogen bonded species	Closest halogen vdW overlap %	Stab. Energy (kcal mol^{-1})
1	$[TeI_6]^{2-}\cdots I_2$ (end-on)	82.1	17.8
2	$[TeI_6]^{2-}\cdots I_2$ (end-on)	83.0	15.4
3	$[TeI_6]^{2-}\cdots I_2$ (end-on)	85.0	13.1
4	$[TeI_6]^{2-}\cdots I_2$	83.7	20.1
5	$[TeI_6]^{2-}\cdots I_3$ (end-on)	91.2	8.91
6	$[TeI_6]^{2-}\cdots$HIPy	98.1	1.58

Analysis of halogen bonding in 1–3: $(HXPy)_2[TeI_6]\cdot I_2$ (X = H, Cl, I)

NBO analyses shed light on the two different types of Te–I$\cdots I_2$ close-contacts in compounds **1–3**. SOPT-calculated stabilization energies for these interactions are listed in Table 3 and isosurface renderings of the NBOs involved shown in Fig. 9. As expected from % vdW overlap, the stronger interaction is between the end-on bound I_2 and the $[TeI_6]^{2-}$ octahedron, with a stabilization energy ranging from 13.2 to 17.5 kcal mol^{-1} in all three complexes (Table 3). The donor NBO consists of a lone pair of electrons on a tellurium-bound iodide, and the acceptor NBO, of an antibonding σ*-type orbital localized on I_2. This end-on interaction can geometrically be considered a type I halogen bond (contact angels $\theta_1 = \theta_2 = \sim 180°$). In the case of end-on halogen bonding in **1–3**, the large stabilization energy and charge transfer character demonstrated by our computational analyses does not strictly meet the definition of a type I interaction. The side-on-I_2–$[TeI_6]^{2-}$ interaction, a bifurcated halogen bond geometrically analogous to a typical type II halogen bond, is significantly weaker, ranging from *ca.* 3.0–4.8 kcal mol^{-1} (Table S1†), with the donor NBOs consisting of I_2 lone pairs and acceptor NBO of a Te–I antibonding σ*-type orbital.

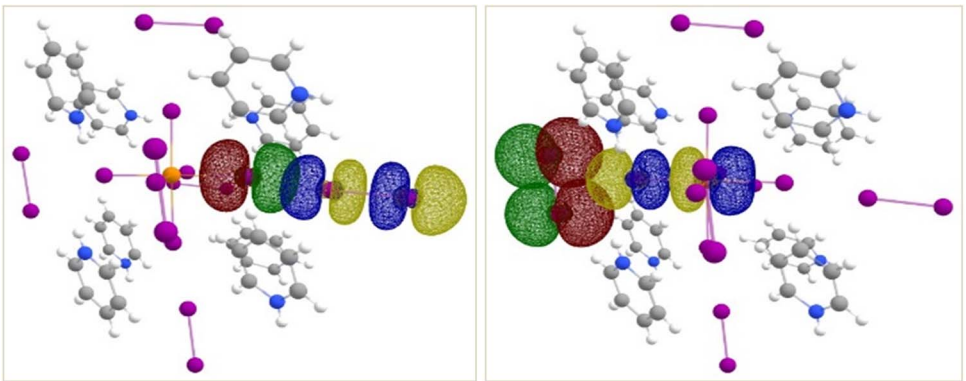

Fig. 9 Isosurface renderings of the NBOs involved in the interactions between end-on bound (left) and side-on bound (right) I_2 molecules and the $[TeI_6]^{2-}$ octahedron in compound **1**. For simplicity, only one of each kind is shown (see text for details). Similar interactions are seen in 2 and 3. Green/red isosurfaces represent donor NBO and blue/yellow isosurfaces represent acceptor NBO.

© 2023 The Author(s). Published by the Royal Society of Chemistry

Open Access Article. Published on 03 May 2023. Downloaded on 2/10/2026 9:29:10 PM.
This article is licensed under a Creative Commons Attribution-NonCommercial 3.0 Unported Licence.

In all three complexes, each $[TeI_6]^{2-}$ octahedron is also surrounded by four side-on bound and two end-on bound I_2 molecules, resulting in non-negligible contributions to overall stabilization energies (Table S1†) from the former. It is worth noting that the nature of this side-on, bifurcated halogen bond is very different in each compound, presumably owing to perturbations introduced by the organic cations and the resulting overall packing of the structures. This is most evidently seen in **3**, in which (a) a weak halogen bond is present between iodopyridine and $[TeI_6]^{2-}$ (% vdW ≈ 97%), and (b) the side-on-I_2–$[TeI_6]^{2-}$ interaction is no longer bifurcated. Also of note is that only a subset of the four I_2 molecules are involved in bifurcated halogen bonding in all three complexes (three in **1**, three in **2** and only one in **3**). These changes in the second sphere environment are most likely due to packing effects of the changing organic cations in **1–3** (HPy > HClPy > HIPy).

Halogen bonding in 4: $(HPyz)_2[TeI_6]\cdot I_2$

Compared to compounds **1–3**, compound **4** exhibits a different second sphere coordination scheme between $[TeI_6]^{2-}$ and I_2 (recall Fig. 3). There are four I_2 molecules engaged in a halogen-bond with the $[TeI_6]^{2-}$ octahedron, with varying Te–I···I_2 distances and Te–I–I_2 angles. Although the atoms involved in halogen-bonding, the % vdW overlap of the closest contacts (Table 3), and the associated donor and acceptor NBOs are all comparable or the same, the geometry of this interaction is quite different compared to those seen in compounds **1–3**. In general, halogen bonds are extremely directional, and this perhaps explains why, at *ca.* 20.1 kcal mol^{-1}, the strongest halogen bond in compound **4** is also the strongest of all six compounds reported here.

Halogen bonding in 5: $(HClPy)_3[TeI_6(I_3)]$

There are two types of $TeI_6^{2-}\cdots I_3^-$ interactions present in compound **5** – end-on and side-on. NBO and SOPT calculations suggest that both these halogen-bonding interactions are approximately equal in strength (*ca.* 9 kcal mol^{-1} and 6 kcal mol^{-1} respectively). Both the end-on and side-on $[TeI_6]^{2-}\cdots I_3^-$ interactions occur *via* the same type of donor and acceptor NBOs (Fig. 10). The donor NBO consists of a lone pair of electrons on an iodine atom of I_3^-, while the acceptor NBO is a Te–I antibonding σ* orbital, reminiscent of the weaker side-on interactions in compounds **1–3**.

Halogen bonding in 6: $(HBrPy)_2[TeI_6]$

Compound **6** is the only compound reported herein that is devoid of any polyiodide species. Halogen bonding interactions do exist between the bromine substituent of the bromopyridinium cation and the $[TeI_6]^{2-}$ octahedron. The SOPT-calculated stabilization energy of the $[HBrPy]^+\cdots[TeI_6]^{2-}$ interaction (3.758(1) Å, 98.1% vdW) is only 2.48 kcal mol^{-1}, and represents the strongest halogen–halogen interaction present in **6** that was included in our computational model. Halogen bonding interactions also exist between adjacent octahedra as illustrated previously, but these interactions were too computationally expensive to be modeled. In **6**, a combination of hydrogen and carbon bonding also contribute to octahedron asymmetry. In **1–5**, the longest Te–I bonds in the $[TeI_6]^{2-}$ octahedron were simply those with the strongest halogen bonding between the tellurium bound halide and the surrounding polyiodides. However in **6**, the longest Te–I bond (3.048(1) xzk Å) is not involved in halogen bonding with the $[HBrPy]^+$ or an adjacent metal halide octahedron. The significant hydrogen and carbon bonding (Fig. 11) between a single tellurium bound iodine and the surrounding pyridinium species have a total stabilization energy of 6.85 kcal mol^{-1}, spread between two different BrPy molecules. Therefore in **6**, hydrogen and carbon bonding interactions trump halogen bonding in their overall stabilization energy and in their influence on the metal halide inner sphere bonding. A summation of stabilization energies for hydrogen, carbon, and halogen bonding in compound **6** can be seen in Table S2.† This 6.85 kcal mol^{-1} stabilization energy, spread over two BrPy, is still smaller than the 8.91 kcal mol^{-1} of the single strongest halogen bond in **5**, and even smaller than those in **1–4**.

Electrostatic surface potential (ESP) maps on the surface of molecules are an additional tool to study noncovalent

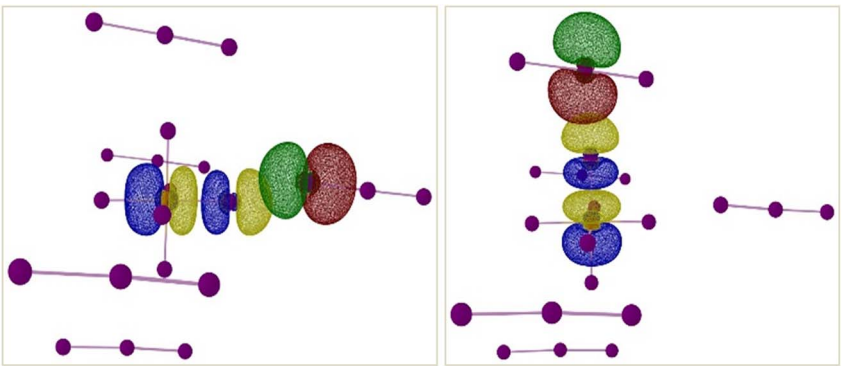

Fig. 10 Isosurface renderings of the NBOs involved in the XB interactions between end-on bound (left) and side-on bound (right) I_3^- and the $[TeI_6]^{2-}$ octahedron in compound **5**. Green/red isosurfaces represent donor NBO and blue/yellow isosurfaces represent acceptor NBO. Counter-cations omitted for clarity.

Open Access Article. Published on 03 May 2023. Downloaded on 2/10/2026 9:29:10 PM. This article is licensed under a Creative Commons Attribution-NonCommercial 3.0 Unported Licence.

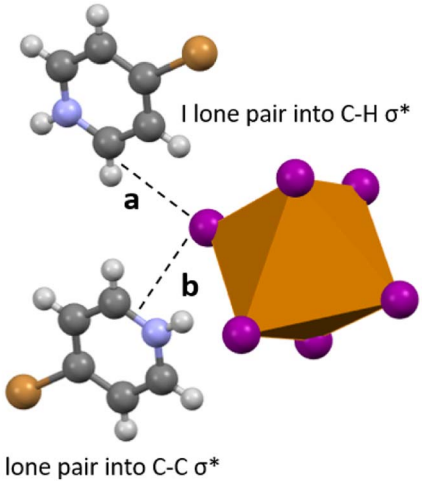

Fig. 11 Selected view of **6**, showing hydrogen bonding (a) and carbon bonding (b) between the $[TeI_6]^{2-}$ and adjacent bromopyridinium cations. Iodine one pairs donate electron density into either a C–H σ* (hydrogen bonding), or C–C or C–N σ* (carbon bonding).

interactions and their role in the assembly of crystalline materials. Complementing the NBO calculations described above, the ESP maps in Fig. 12 adequately rationalize both the different modes of halogen bonding between $[TeI_6]^{2-}$ and I_2 or I_3^-, and their relative strengths. For compounds **1–4**, in cases where the donor NBO is based on a Te-bound iodide, the most electron-rich portion of the $[TeI_6]^{2-}$ octahedron (molecular electrostatic potential (MEP) energy plotted on a 0.002 ε·bohr^{-1} isodensity surface = −161.6 kcal mol^{-1}) is sterically inaccessible to the neighboring I_2 molecules. As a consequence, there is a clear trend in interaction energies as a function of the Te–I–I angles. The Te–I···I_2 distances and Te–I–I angles for the strongest halogen bonds (XBs) in **1–4** are as follows: 3.252(1) Å, 167.4° [**1**]; 3.287(1) Å, 161.1° [**2**]; 3.367 Å(1), 151.6° [**3**]; 3.315(1) Å, 101.7° for [**4**]. As the most electrophilic region of I_2 (MEP = 43.2 kcal mol^{-1}) approaches the nucleophilic $[TeI_6]^{2-}$ octahedron, the largest difference in MEPs is achieved as Te–I–I angle approaches 90°, typical of a type-II XB. The directional nature of the weaker bifurcated XB in **1–3**, where I_2 acts as the nucleophile, is also readily seen from Fig. 13. In compound **5**, the orientation of the nucleophilic region (min, max MEP = −96.3 kcal mol^{-1}, −90.1 kcal mol^{-1}) local to the central iodine towards the $[TeI_6]^{2-}$ octahedron results in the side-on binding mode of I_3^- shown in Fig. 10. The arrangement of iodine atoms in the end-on bound I_3^- is intriguing as there are two different I–I bond lengths in I_3^-. Let us consider the three distinct I atoms involved, referred to hereafter as I_a, I_b, and I_c (Fig. S20†). In our model, the two I–I distances are slightly uneven, with (I_a—I_b) *ca.* 2.86 Å and (I_b—I_c) at *ca.* 2.97 Å (typical of I_3^- in the solid state).[58] An isodensity surface of 0.002 au around I_a has a maximal MEP value of *ca.* −71.1 kcal mol^{-1}, while I_c has

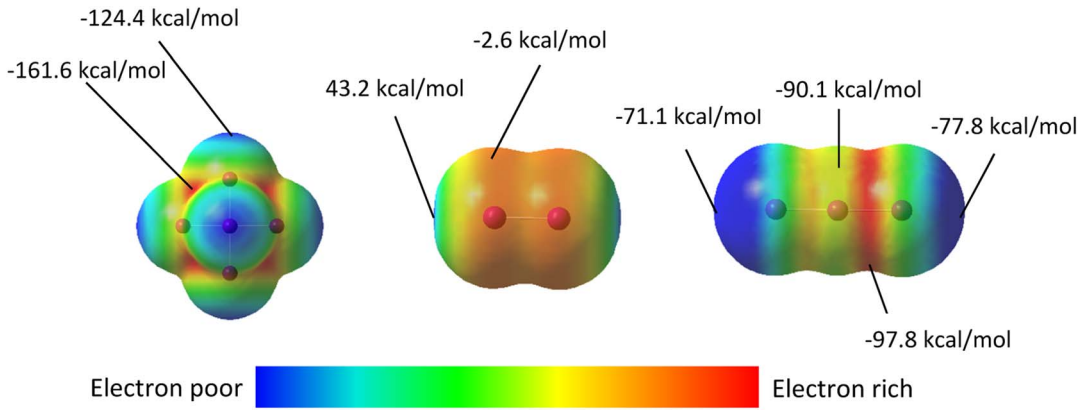

Fig. 12 Electrostatic potential maps of: the $[TeI_6]^{2-}$ (left), I_2 (middle), and I_3^- (right) with highest and lowest electrostatic potentials labeled. Blue indicates electron poor regions, while red indicates regions rich in electron density. ESP surfaces were calculated from geometry optimized molecular species. Note: Color gradients are specific to each molecule, not global. ESP energies represent what a unit positive charge would experience at that point on the surface.

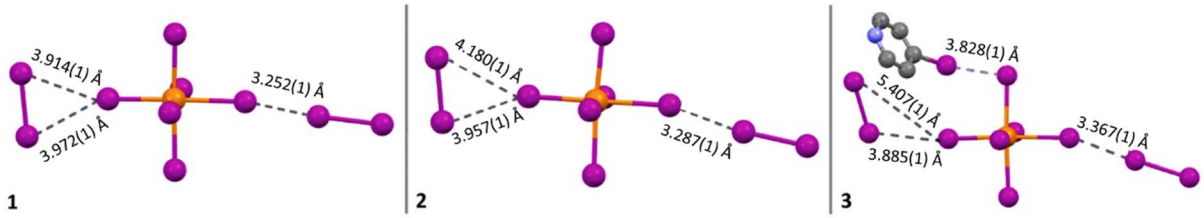

Fig. 13 Most significant halogen bonds in compounds **1–3**, which include end-on and side-on I···I bonds geometrically matching type I and II halogen bonds respectively.

© 2023 The Author(s). Published by the Royal Society of Chemistry

Open Access Article. Published on 03 May 2023. Downloaded on 2/10/2026 9:29:10 PM.
This article is licensed under a Creative Commons Attribution-NonCommercial 3.0 Unported Licence.

a maximal value of −77.8 kcal mol^{-1}. It is interesting to note that it is I_a, and not I_c, that is oriented towards the $[TeI_6]^{2-}$ octahedron. While this may seem at odds with the e$^-$-donor nature of I_3^-, it is to be noted that each I_3^- unit is involved in four XBs at the same time (see Fig. S18†). Our simplified models for NBO analyses have included only one such interaction per I_3^-; a more extensive model would perhaps account for this behavior.

Whereas NBO calculations and ESP maps shed light on individual NCIs within our selected molecular models, DOS calculations (applying periodic boundary conditions) were also performed to highlight atomic contributions to the frontier crystal orbitals, and to support experimental bandgap measurements. In all six compounds, the frontier orbitals in the valence band are dominated by $[TeI_6]^{2-}$. An obvious difference between **1–5** and **6** is the presence of I_2 or I_3^- in the former, while the latter lacks any polyiodide species. This has a clear effect on electronic structure, as can be seen from the sizeable contributions of I_2/I_3^- to the valence band of **1–5**, particularly closer to the band edge (Fig. 14). Similar contributions by polyiodide species are seen in the conduction band as well, except for the case of **4**, for which the counter-cation, being a pyrazinium instead of a pyridinium, has its π* orbitals interspersed between the valence band and orbitals of TeI_6^{2-} and I_2. Also of note is the negligible contribution of the more electronegative chloro- and bromo-substituted pyridiniums to the valence band. I_{HIPy}-based orbitals, owing to the more electropositive nature of iodine, have some minor contributions near the band edge.

Unlike in our previous work with tellurium chlorides and bromides,[4] as well as antimony halides,[19] we find here that the 'intermediate bands' just below the bulk of the conduction band are composed entirely of Te, I_{Te-I} and I_2/I_3^- orbitals, and have no contribution from π* orbitals of the organic cations, except in the case of **4**. In **5**, I_3^- orbitals and chloropyridinium π* orbitals are found in the conduction band edge. Whereas in **6**, bromopyridinium π* orbitals dominate the lowest unoccupied orbitals, there is a non-negligible contribution from the $[TeI_6]^{2-}$ units.

Bandgap measurements by diffuse reflectence spectroscopy

Fig. 15 shows a combination of diffuse reflectance spectra for **1–4**, **6**, and **8**. The I_2-containing materials (**1–4**) have the lowest energy bandgaps (1.0–1.17 eV) of the set. Previously reported $[TeBr_6]^{2-}$ containing I_2 species have higher energy bandgaps in the range of 1.4–1.5 eV (826–885 nm).[59] Compound **6** $(BrPy)_2[TeI_6]$ (green in Fig. 15) exhibits a bandgap of 1.42 eV, significantly higher in energy than **1–4**. Compound **5** could not be produced in a reasonably pure state, and is therefore was not included in these measurements. The bandgaps of (HClPy)[I_3]·

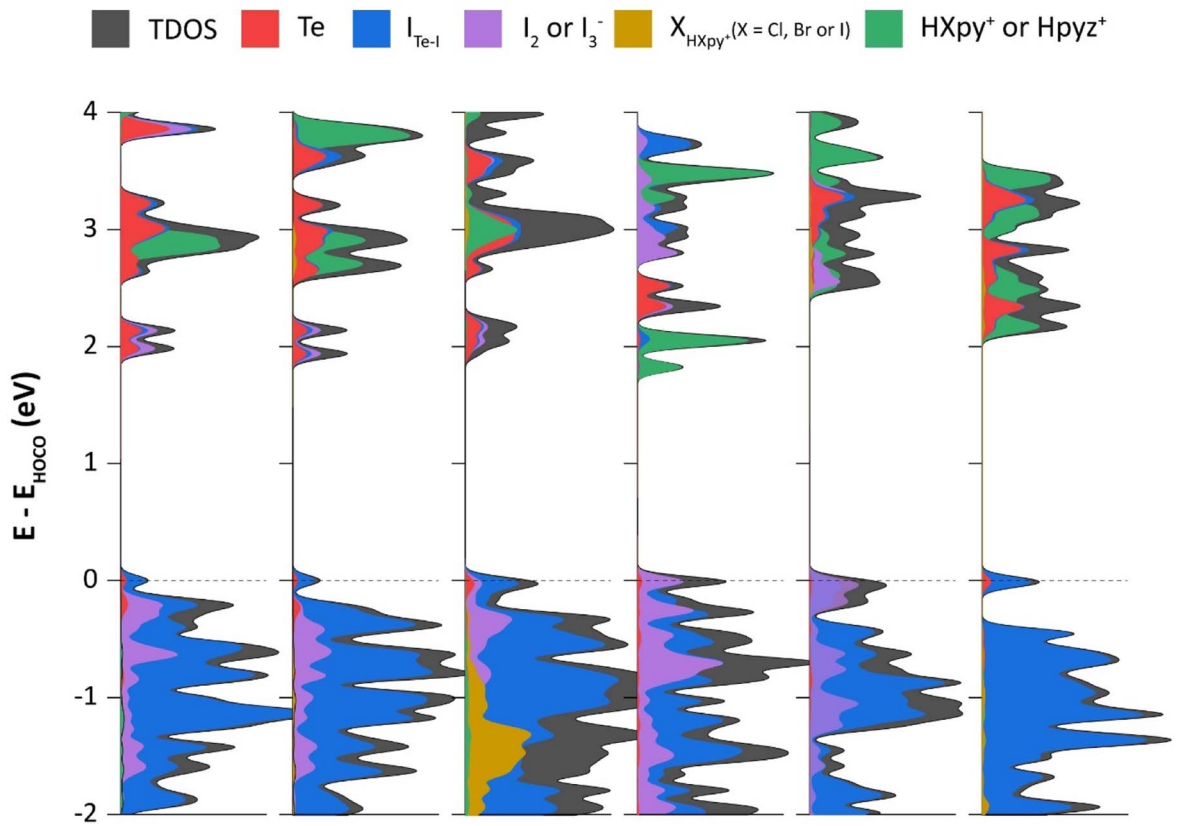

Fig. 14 Density of states (*x*-axis) of compounds **1–6** projected onto atomic orbitals of Te (s and p), I_{Te-I} (s and p), I_2 or I_3^- (s and p), X_{HXpy+} (X = Cl, Br or I), and $HXpy^+/Hpyz^+$; I_{Te-I} = Te-bound I atoms, X_{HXpy+} = halogen atoms in respective halopyridinium cations, and pyz = pyrazine. Dashed line at 0 eV represents the valence band edge (HOCO, highest occupied crystal orbital).

Open Access Article. Published on 03 May 2023. Downloaded on 2/10/2026 9:29:10 PM. This article is licensed under a Creative Commons Attribution-NonCommercial 3.0 Unported Licence.

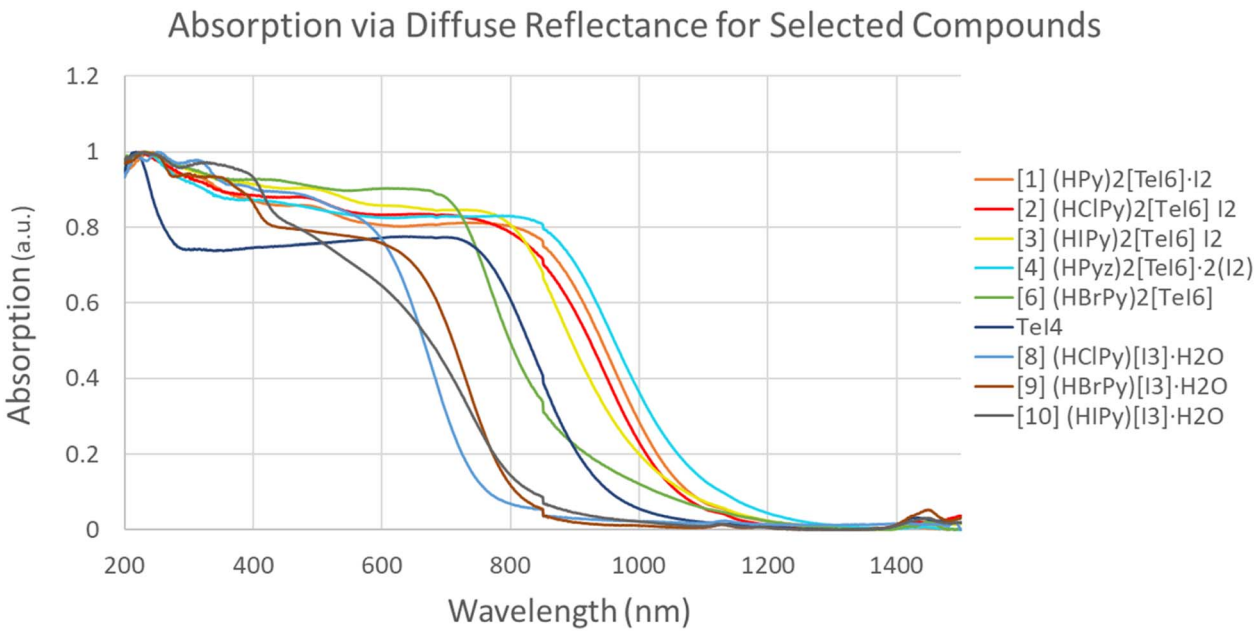

Fig. 15 Normalized diffuse reflectance measurements for **1–4**, **6**, **8–10** and TeI_4.

Table 4 Optical bandgaps calculated from diffuse reflectance spectra from Fig. 15, and DFT-calculated bandgaps

Compound	Bandgap expt. (eV)	Bandgap DFT (eV)
[**1**] $(HPy)_2[TeI_6]\cdot I_2$	1.20	1.71
[**2**] $(HClPy)_2[TeI_6]\cdot I_2$	1.21	1.86
[**3**] $(HIPy)_2[TeI_6]\cdot I_2$	1.25	1.82
[**4**] $(HPyz)_2[TeI_6]\cdot 2(I_2)$	1.18	1.54
[**6**] $(HBrPy)_2[TeI_6]$	1.42	2.12
TeI_4	1.36	—
[**8**] $(HClPy)[I_3]\cdot H_2O$	1.71	—

H_2O and TeI_4 (Fig. 15 and Table 4) are shown to be 1.71 and 1.36 eV respectively, both higher in energy than each of the I_2 containing compounds. These data suggest that the presence of I_2 (in **1–4**) and robust halogen bonding substantially affects the band gap of these materials. These results fit with our crystallographic metrics, with **1–4** exhibiting halogen bonding with a relatively large vdW overlap, and our computational metrics showing relatively high stabilization energies for $[TeI_6]^{2-}\cdots I_2$ halogen bonds.

Compiled metrics

A collection of the computational and crystallographic metrics presented so far can be seen in Fig. 16. $[TeI_6]^{2-}$ octahedra generally tend to become more asymmetric with stronger halogen bonds (lower vdW %, Fig. 16a). Within compounds **1–3**, the size of the halogen substituent on the pyridinium appears to affect the vdW overlap, with the closest I···I contact (lowest % vdW) and highest distortion of the $[TeI_6]^{2-}$ belonging to **1**, with less overlap (higher % vdW) in **2** and **3**. Compounds **1–5** as a group also generally fit this trend, albeit less neatly than the subset of **1–3**. **6** is expected to be an outlier in this case, having no polyiodides present. The dominance of hydrogen and carbon bonding over halogen bonding in **6**, as seen from their relative stabilization energies, also contributes to its status as an outlier in this case. Stabilization energy in halogen bonding interactions increases with closer second sphere halogen–halogen interactions (low vdW overlap %, Fig. 16b). The highest stabilization energy for a halogen–halogen interaction belongs to **4**, which is slightly larger than that for **1** or **2**. In **1–4**, a lower energy bandgap correlates with a more intimate vdW overlap, again indicating that relatively strong halogen bonding with polyiodide species lower the bandgap of 0 dimensional tellurium iodides relative to materials, namely compound **6**, without such species (Fig. 16c and d). A plot of calculated bandgap *vs.* stabilization energy is present in Fig. S21.†

Elemental analysis

Results of elemental analysis (Table S3†) ranged from good agreement with theoretical values (compounds **4** and **5**) to expectedly off (compounds **1–3**, **6**, **7–10**). Excepting 4 and 5, most compounds exhibited lower than theoretical iodine content and conversely higher than expected C, H, N content. We ascribe this discrepancy to the impurity phases explicity identified by PXRD (*e.g.* TeI_4 or iodide salts of pyridinium) as well as the volatilization of I_2, evidenced by the brownish purple coloration of sample containers. The percent compositons of impurity phases have been tabulated in Fig. S4.† We note that the PXRD for compounds **4** and **5** (Fig. S4 and S6–S8†) revealed the presence of significant impurity phases, which did not seem to be reflected in the elemental anlysis results. Elemental analysis of compound **7** was predictably off-base, being

© 2023 The Author(s). Published by the Royal Society of Chemistry

Open Access Article. Published on 03 May 2023. Downloaded on 2/10/2026 9:29:10 PM.
This article is licensed under a Creative Commons Attribution-NonCommercial 3.0 Unported Licence.

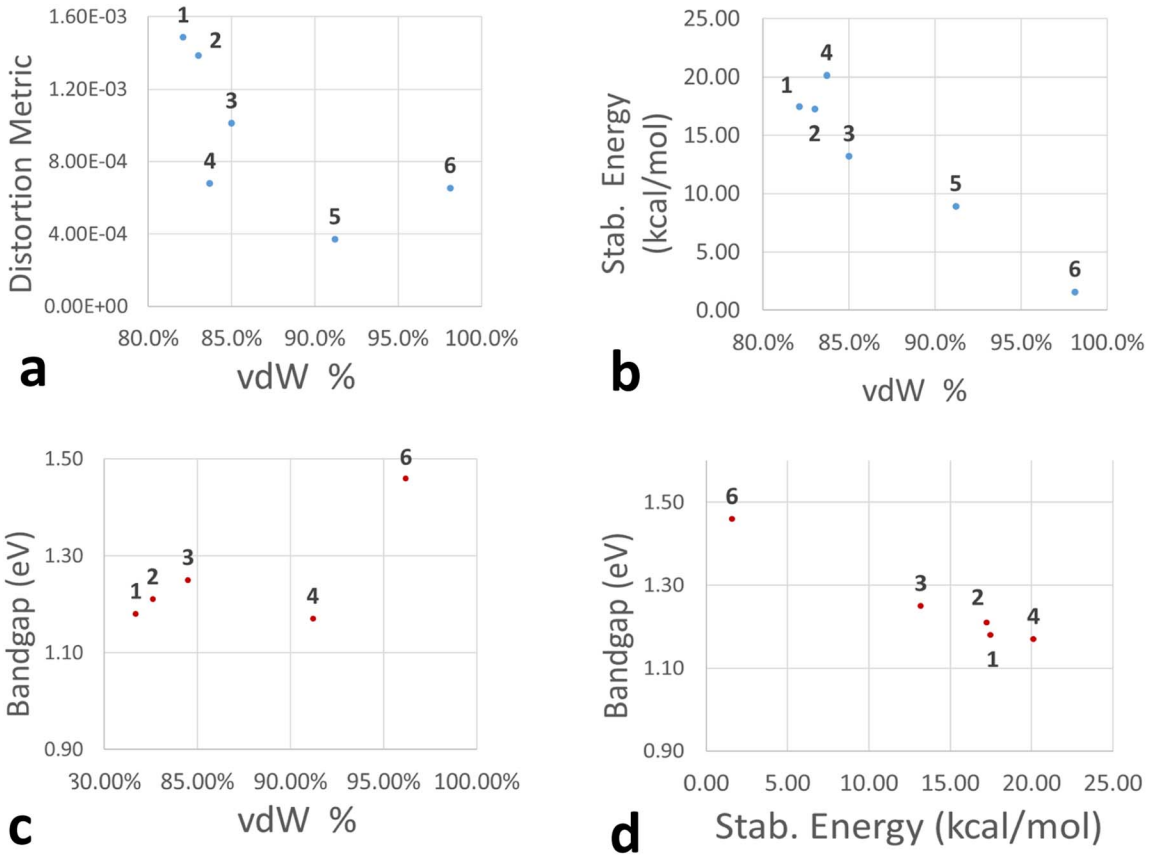

Fig. 16 Plots showing correlation of distortion metric (a), vdW % overlap (a–c), stabilization energy (kcal mol^{-1}, b and d), and bandgap (eV, c and d) of the most intimate halogen bond in **1–6**.

a minority phase grown by evaporation on glass slides, as stated in the experimental section.

Conclusions

We have presented a family of tellurium based halide perovskite derivatives and have evaluated the role of non-covalent interactions, mainly halogen bonding, in their assembly and material properties. Close contacts between $[TeI_6]^{2-}$ and polyiodide species occur in **1–5**, with crystallographic metrics indicating strong halogen bonding. Computational metrics reinforce this assertion, with **1–5** exhibiting stabilization energies of 10–15 kcal mol^{-1} between $[TeI_6]^{2-}$ and I_2 or I_3^- species, as determined by NBO and SOPT analyses. This relatively robust halogen bonding between the $[TeI_6]^{2-}$ and polyiodide species seems to exacerbate the asymmetry of the metal halide octahedron, with greater vdW overlap correlating with octahedral asymmetry. Furthermore, the presence of I_2 and the resulting halogen bonding directly affect the bandgap of the material, lowering it compared to materials without polyiodide species (compounds **1–4** *vs.* **6**). Within **1–3**, the size of the halogen substituent on the XPy affects the vdW overalp of the $[TeI_6]^{2-}\cdots I_2$ pair, with the overlap decreasing (higher vdW %) with increasing halogen size. **1–3** also exhibit a very similar second sphere interaction geometry, with 6 I_2 halogen bonding with each $[TeI_6]^{2-}$ octahedron. In **6**, a combination of hydrogen and carbon bonding contribute to octahedral asymmetry, with the longest Te–I bond in the $[TeI_6]^{2-}$ participating in said bonding. Hydrogen and carbon bonding between a single iodine of the $[TeI_6]^{2-}$ octahedron and the surrounding pyridinium species have a stabilization energy of 6.85 kcal mol^{-1}, more than the halogen bonding stabilization energy of 1.58 kcal mol^{-1} in the same compound. Future work could center around evaluating how the inner sphere of different metal halides are influenced by the relatively strong second sphere halogen bonds involving polyiodides. It is an open question how other perovskite-relevant metal halides, Sn or Bi halides *e.g.*, would behave in the presence of polyiodide species.

Conflicts of interest

There are no conflicts to declare.

Acknowledgements

This material is based upon work supported by the Department of Energy National Nuclear Security Administration through the Nuclear Science and Security Consortium under Award Number DE-NA0003180. This report was prepared as an account of work sponsored by an agency of the United States Government.

Open Access Article. Published on 03 May 2023. Downloaded on 2/10/2026 9:29:10 PM. This article is licensed under a Creative Commons Attribution-NonCommercial 3.0 Unported Licence.

Neither the United States Government nor any agency thereof, nor any of their employees, makes any warranty, express or limited, or assumes any legal liability or responsibility for the accuracy, completeness, or usefulness of any information, apparatus, product, or process disclosed, or represents that its use would not infringe privately owned rights. Reference herein to any specific commercial product, process, or service by trade name, trademark, manufacturer, or otherwise does not necessarily constitute or imply its endorsement, recommendation, or favoring by the United States Government or any agency thereof. The views and opinions of authors expressed herein do not necessarily state or reflect those of the United States Government or any agency thereof. This work was completed in part with resources provided by the High Performance Computing Cluster at The George Washington University, Research Technology Services.

References

1 B. A. Connor, R. I. Biega, L. Leppert and H. I. Karunadasa, Dimensional reduction of the small-bandgap double perovskite Cs2AgTlBr6, *Chem. Sci.*, 2020, **11**, 7708–7715.
2 M. D. Smith, E. J. Crace, A. Jaffe and H. I. Karunadasa, The diversity of layered halide perovskites, *Annu. Rev. Mater. Res.*, 2018, **48**, 111–136.
3 S. Zhao, W. Cai, H. Wang, Z. Zang and J. Chen, All-inorganic lead-free perovskite(-like) single crystals: synthesis, properties, and applications, *Small Methods*, 2021, **5**, 1–35.
4 A. D. Nicholas, B. W. Walusiak, L. C. Garman, M. N. Huda and C. Cahill, Impact of noncovalent interactions on structural and photophysical properties of zero-dimensional tellurium(IV) perovskites, *J. Mater. Chem. C*, 2021, 3271–3286, DOI: 10.1039/d0tc06000c.
5 P. R. Varadwaj, A. Varadwaj, H. M. Marques and K. Yamashita, Significance of hydrogen bonding and other noncovalent interactions in determining octahedral tilting in the $CH_3NH_3PbI_3$ hybrid organic-inorganic halide perovskite solar cell semiconductor, *Sci. Rep.*, 2019, **9**, 1–30.
6 P. Metrangolo, L. Canil, A. Abate, G. Terraneo and G. Cavallo, Halogen bonding in perovskite solar cells: a new tool for improving solar energy conversion, *Angew. Chem Int., Ed.*, 2021, **61**(11), e202114793.
7 J. Guo, Y. Xu, W. Yang, B. Xiao, Q. Sun, X. Zhang, B. Zhang, M. Zhu and W. Jie, High-stability flexible X-ray detectors based on lead-free halide perovskite Cs2TeI6Films, *ACS Appl. Mater. Interfaces*, 2021, **13**, 23928–23935.
8 Y. Xu, B. Jiao, T. B. Song, C. C. Stoumpos, Y. He, I. Hadar, W. Lin, W. Jie and M. G. Kanatzidis, Zero-dimensional Cs 2 TeI 6 Perovskite: solution-processed thick films with high x-ray sensitivity, *ACS Photon.*, 2019, **6**, 196–203.
9 S. Nagorny, Novel Cs_2HfC_{l6} Crystal scintillator: recent progress and perspectives, *Physics*, 2021, **3**, 320–351.
10 R. Zhang, X. Mao, Y. Yang, S. Yang, W. Zhao, T. Wumaier, D. Wei, W. Deng and K. Han, Air-stable, lead-free zero-dimensional mixed bismuth-antimony perovskite single crystals with ultra-broadband emission, *Angew. Chem., Int. Ed.*, 2019, **58**, 2725–2729.
11 J. Almutlaq, J. Yin, O. F. Mohammed and O. M. Bakr, The benefit and challenges of zero-dimensional perovskites, *J. Phys. Chem. Lett.*, 2018, **9**, 4131–4138.
12 Z. Tan, J. Pang, G. Niu, J. H. Yuan, K. H. Xue, X. Miao, W. Tao, H. Zhu, Z. Li, H. Zhao, X. Du and J. Tang, Tailoring the electron and hole dimensionality to achieve efficient and stable metal halide perovskite scintillators, *Nanophotonics*, 2021, **10**, 2249–2256.
13 R. Chiara, M. Morana, M. Boiocchi, M. Coduri, M. Striccoli, F. Fracassi, A. Listorti, A. Mahata, P. Quadrelli, M. Gaboardi, C. Milanese, L. Bindi, F. De Angelis and L. Malavasi, Role of spacer cations and structural distortion in two-dimensional germanium halide perovskites, *J. Mater. Chem. C*, 2021, **9**, 9899–9906.
14 Y. Han, S. Yue and B. B. Cui, Low-dimensional metal halide perovskite crystal materials: structure strategies and luminescence applications, *Adv. Sci.*, 2021, **8**, 1–21.
15 K. M. McCall, V. Morad, B. M. Benin and M. V. Kovalenko, Efficient lone-pair-driven luminescence: structure-property relationships in emissive 5s2Metal halides, *ACS Mater. Lett.*, 2020, **2**, 1218–1232.
16 P. Metrangolo, IUPAC definition of the halogen bond, *Acta Crystallogr., Sect. A: Found. Adv.*, 2017, **73**, C309.
17 P. Metrangolo, F. Meyer, T. Pilati, G. Resnati and G. Terraneo, Halogen bonding in supramolecular chemistry, *Angew. Chem., Int. Ed.*, 2008, **47**, 6114–6127.
18 B. Inscoe, H. Rathnayake and Y. Mo, Role of charge transfer in halogen bonding, *J. Phys. Chem. A*, 2021, **125**, 2944–2953.
19 A. D. Nicholas, R. N. Halli, L. C. Garman and C. L. Cahill, Low-dimensional hybrid indium/antimony halide perovskites: supramolecular assembly and electronic properties, *J. Phys. Chem. C*, 2020, **124**, 25686–25700.
20 H. A. Evans, J. L. Andrews, D. H. Fabini, M. B. Preefer, G. Wu, A. K. Cheetham, F. Wudl and R. Seshadri, The capricious nature of iodine catenation in I2 excess, perovskite-derived hybrid Pt(IV) compounds, *Chem. Commun.*, 2019, **55**, 588–591.
21 G. Braathen and H. F. Pi-Tai Chou, Time-Resolved reaction of O_2 with I- in aqueous solution, *J. Phys. Chem.*, 1988, 6610–6615.
22 Q. Sun, X. Gong, H. Li, S. Liu, X. Zhao, Y. Shen and M. Wang, Direct formation of I3- ions in organic cation solution for efficient perovskite solar cells, *Sol. Energy Mater. Sol. Cells*, 2018, **185**, 111–116.
23 *SAINT Version 8.34a*, Bruker AXS Inc., Madison.
24 G. M. Sheldrick, *SADABS*, University of Göttingen, Germany, 2007.
25 G. M. Sheldrick, A short history of SHELX, *Acta Crystallogr., Sect. A: Found. Crystallogr.*, 2008, **64**, 112–122.
26 C. B. Hübschle, G. M. Sheldrick and B. S. X. Dittrich, A Qt graphical user interface for SHELXL, *J. Appl. Crystallogr.*, 2011, **44**, 1281–1284.
27 O. V. Dolomanov, L. J. Bourhis, R. J. Gildea, J. A. K. Howard and H. Puschmann, OLEX2: a complete structure solution, refinement and analysis program, *J. Appl. Crystallogr.*, 2009, **42**, 339–341.

© 2023 The Author(s). Published by the Royal Society of Chemistry

Open Access Article. Published on 03 May 2023. Downloaded on 2/10/2026 9:29:10 PM. This article is licensed under a Creative Commons Attribution-NonCommercial 3.0 Unported Licence.

28 A. L. Spek, Single-crystal structure validation with the program PLATON, *J. Appl. Crystallogr.*, 2003, **36**, 7–13.
29 M. Burnett and C. Johnson, *ORTEP-III: Oak Ridge Thermal Ellipsoid Plot Program for Crystal Structure Illustrations Oak Ridge National Laboratory Report ORNL-6895*, 1996.
30 S. Parsons, Introduction to twinning, *Acta Crystallogr., Sect. D: Biol. Crystallogr.*, 2003, **59**, 1995–2003.
31 M. J. Frisch, G. W. Trucks, H. B. Schlegel, G. E. Scuseria, M. a. Robb, J. R. Cheeseman, G. Scalmani, V. Barone, G. a. Petersson, H. Nakatsuji, X. Li, M. Caricato, a. V. Marenich, J. Bloino, B. G. Janesko, R. Gomperts, B. Mennucci, H. P. Hratchian, J. V. Ortiz, a. F. Izmaylov, J. L. Sonnenberg, F. Williams Ding, F. Lipparini, F. Egidi, J. Goings, B. Peng, A. Petrone, T. Henderson, D. Ranasinghe, V. G. Zakrzewski, J. Gao, N. Rega, G. Zheng, W. Liang, M. Hada, M. Ehara, K. Toyota, R. Fukuda, J. Hasegawa, M. Ishida, T. Nakajima, Y. Honda, O. Kitao, H. Nakai, T. Vreven, K. Throssell, J. a. Montgomery Jr., J. E. Peralta, F. Ogliaro, M. J. Bearpark, J. J. Heyd, E. N. Brothers, K. N. Kudin, V. N. Staroverov, T. a. Keith, R. Kobayashi, J. Normand, K. Raghavachari, a. P. Rendell, J. C. Burant, S. S. Iyengar, J. Tomasi, M. Cossi, J. M. Millam, M. Klene, C. Adamo, R. Cammi, J. W. Ochterski, R. L. Martin, K. Morokuma, O. Farkas, J. B. Foresman and D. J. Fox, *G16_C01. Gaussian 16, Revision C.01*, Gaussian, Inc., Wallin at, 2016.
32 A. D. Beck, Density-functional thermochemistry. III. The role of exact exchange, *J. Chem. Phys.*, 1993, **98**, 5648–5656.
33 T. Lecklider, Maintainng a heathy rhythm, *Eval. Eng.*, 2011, **50**, 36–39.
34 F. Weigend, Accurate coulomb-fitting basis sets for H to Rn, *Phys. Chem. Chem. Phys.*, 2006, **8**, 1057–1065.
35 F. Weigend and R. Ahlrichs, Balanced basis sets of split valence, triple zeta valence and quadruple zeta valence quality for H to Rn: design and assessment of accuracy, *Phys. Chem. Chem. Phys.*, 2005, **7**, 3297–3305.
36 A. V. Krukau, O. A. Vydrov, A. F. Izmaylov and G. E. Scuseria, Influence of the exchange screening parameter on the performance of screened hybrid functionals, *J. Chem. Phys.*, 2006, **125**(22), 224106.
37 R. Krishnan, J. S. Binkley, R. Seeger and J. A. Pople, Self-consistent molecular orbital methods. XX. A basis set for correlated wave functions, *J. Chem. Phys.*, 1980, **72**, 650–654.
38 A. D. McLean and G. S. Chandler, Contracted Gaussian basis sets for molecular calculations. I. Second row atoms, Z=11-18, *J. Chem. Phys.*, 1980, **72**, 5639–5648.
39 T. Lu and F. M. Chen, A multifunctional wavefunction analyzer, *J. Comput. Chem.*, 2012, **33**, 580–592.
40 G. Cavallo, P. Metrangolo, R. Milani, T. Pilati, A. Priimagi, G. Resnati and G. Terraneo, The halogen bond, *Chem. Rev.*, 2016, **116**, 2478–2601.
41 E. Faoro, G. M. de Oliveira, E. S. Lang and C. B. Pereira, Synthesis and structural features of new aryltellurenyl iodides, *J. Organomet. Chem.*, 2010, **695**, 1480–1486.
42 A. Bondi, Van der waals volumes and radii, *J. Phys. Chem.*, 1964, **68**, 441–451.
43 D. Meggiolaro, E. Mosconi and F. De Angelis, Modeling the Interaction of Molecular Iodine with MAPbI3: a probe of lead-halide perovskites defect chemistry, *ACS Energy Lett*, 2018, **3**, 447–451.
44 L. Lanzetta, T. Webb, N. Zibouche, X. Liang, D. Ding, G. Min, R. J. E. Westbrook, B. Gaggio, T. J. Macdonald, M. S. Islam and S. A. Haque, Degradation mechanism of hybrid tin-based perovskite solar cells and the critical role of tin(IV) iodide, *Nat. Commun.*, 2021, **12**, 1–11.
45 N. A. Belich, A. A. Petrov, P. O. Rudnev, N. M. Stepanov, I. Turkevych, E. A. Goodilin and A. B. Tarasov, From metallic lead films to perovskite solar cells through lead conversion with polyhalide solutions, *ACS Appl. Mater. Interfaces*, 2020, **12**, 20456–20461.
46 D. Quiñonero, Sigma-hole carbon-bonding interactions in carbon-carbon double bonds: An unnoticed contact, *Phys. Chem. Chem. Phys.*, 2017, **19**, 15530–15540.
47 V. Morad, Y. Shynkarenko, S. Yakunin, A. Brumberg, R. D. Schaller and M. V. Kovalenko, Disphenoidal zero-dimensional lead, tin, and germanium halides: highly emissive singlet and triplet self-trapped excitons and X-ray scintillation, *J. Am. Chem. Soc.*, 2019, **141**(25), 9764–9768.
48 X. Wang, W. Meng, W. Liao, J. Wang, R. G. Xiong and Y. Yan, Atomistic mechanism of broadband emission in metal halide perovskites, *J. Phys. Chem. Lett.*, 2019, **10**, 501–506.
49 M. E. Sun, T. Geng, X. Yong, S. Lu, L. Ai, G. Xiao, J. Cai, B. Zou and S. Q. Zang, Pressure-triggered blue emission of zero-dimensional organic bismuth bromide perovskite, *Adv. Sci.*, 2021, **8**, 1–7.
50 M. T. Casais, I. Laue-langevin, F.-G. Cedex and R. V. August Evolution of the Jahn - Teller distortion of MnO_6 octahedra in RMnO3 perovskites (R) Pr, Nd, Dy, Tb, Ho, Er, Y): a neutron diffraction study. 917–923 (2000).
51 T. V. Sedakova, A. G. Mirochnik and V. E. Karasev, Structure and luminescence properties of tellurium(IV) complex compounds, *Opt. Spectrosc.*, 2011, **110**, 755–761.
52 P. C. Srivastava, S. Bajpai, S. Bajpai, C. Ram, R. Kumar, J. P. Jasinski and R. J. T. Butcher, Potential synthons for charge-transfer complexes (involving hypervalent Te-I bonds) and serendipitous synthesis of the first triphenyl methyl phosphonium salts containing $[C_4H_8TeI_4]2-$ and $[TeI_6]2$-anions, *J. Organomet. Chem.*, 2004, **689**, 194–202.
53 S. M. Närhi, R. Oilunkaniemi and R. S. Laitinen, Crystal structure of bis[(5-oxooxolan-3-yl)triphenylphosphanium] hexaiodidotellurate(IV), *Acta Crystallogr., Sect. E: Struct. Rep.*, 2014, **70**.
54 T. V. Sedakova and A. G. Mirochnik, Luminescent and thermochromic properties of tellurium(IV) halide complexes with cesium, *Opt. Spectrosc.*, 2016, **120**, 268–273.
55 A. E. Maughan, A. M. Ganose, M. M. Bordelon, E. M. Miller, D. O. Scanlon and J. R. Neilson, Defect tolerance to intolerance in the vacancy-ordered double perovskite semiconductors Cs_2SnI_6 and Cs_2TeI_6, *J. Am. Chem. Soc.*, 2016, **138**, 8453–8464.
56 D. Ju, X. Zheng, J. Yin, Z. Qiu, B. Türedi, X. Liu, Y. Dang, B. Cao, O. F. Mohammed, O. M. Bakr and X. Tao, Tellurium-based double perovskites A2TeX6 with tunable

Open Access Article. Published on 03 May 2023. Downloaded on 2/10/2026 9:29:10 PM.
This article is licensed under a Creative Commons Attribution-NonCommercial 3.0 Unported Licence.

band gap and long carrier diffusion length for optoelectronic applications, *ACS Energy Lett.*, 2019, **4**, 228–234.

57 S. A. Adonin, A. N. Usoltsev, A. S. Novikov, B. A. Kolesov, V. P. Fedin and M. N. Sokolov, One- and two-dimensional iodine-rich iodobismuthate(III) complexes: structure, optical properties, and features of halogen bonding in the solid state, *Inorg. Chem.*, 2020, **59**, 3290–3296.

58 F. Groenewald, C. Esterhuysen and J. Dillen, Extensive theoretical investigation: Influence of the electrostatic environment on the $I_3^-\cdots I_3^-$ anion-anion interaction, *Theor. Chem. Acc.*, 2012, **131**, 1–12.

59 A. V. Novikov, A. N. Usoltsev, S. A. Adonin, A. A. Bardin, D. G. Samsonenko, G. V. Shilov, M. N. Sokolov, K. J. Stevenson, S. M. Aldoshin, V. P. Fedin and P. A. Troshin, Tellurium complex polyhalides: narrow bandgap photoactive materials for electronic applications, *J. Mater. Chem. A*, 2020, **8**, 21988–21992.

© 2023 The Author(s). Published by the Royal Society of Chemistry